# Performance Analysis of NOMA-Enabled RIS-Assisted Backscatter Communication

Muhammad Usman, *Student Member, IEEE,* Sarah Basharat, *Student Member, IEEE,* Syed Ali Hassan, *Senior Member, IEEE,* Haris Pervaiz, *Member, IEEE,* Zhiguo Ding, *Fellow, IEEE,* and Haejoon Jung, *Senior Member, IEEE*

***Abstract*—Backscatter communication (BackCom), which allows the passive wireless sensors to transmit via modulation and reflection of an incident radio-frequency (RF) signal, is a promising solution for the sustained operation of Internet-of-Things (IoT) nodes. Moreover, to address the inherent coverage and data rate limitations of contemporary BackCom systems, reconfigurable intelligent surfaces (RISs) have come to the forefront for the adaptive configuration of wireless environments. Meanwhile, BackCom systems can incorporate non-orthogonal multiple access (NOMA) to achieve higher spectral efficiency for massive connectivity. Hence, we consider a NOMA-enabled bistatic BackCom system, where multiple backscatter nodes (BSNs) are grouped by the NOMA principle and served with the assistance of an RIS. Using the method of moments (MoM), we analyze and obtain the bit error rate (BER) expressions of a 2-BSN NOMA cluster under imperfect successive interference cancellation (SIC). The validity of the derived expressions is corroborated through extensive numerical simulations. Furthermore, the performance of the proposed system is evaluated in comparison with the conventional NOMA-BackCom system. Our results reveal the superior performance of the RIS-assisted NOMA system, and demonstrate the influence of the number of RIS elements and the choice of reflection coefficients on the BER performance of the proposed system.**

***Index Terms*—Backscatter communication, non-orthogonal multiple access, reconfigurable intelligent surface, bit error rate, method of moments.**

## I. Introduction

The sixth generation (6G) of communication systems is focused on the provision of ultra-low latency, extremely high data rates, and enhanced spectral efficiency for enabling the multifarious paradigms of wireless communications, whilst conforming to the energy requirements of the next-generation cyber-physical applications [2]. These applications mandate the surveillance, management, actuation, and control of a diverse set of processes, built upon complex machine-to-machine (M2M) network architectures [3]. Massive Internet-of-Things (IoT) networks for 6G are expected to accommodate ubiquitous connectivity among the plethora of diverse devices with limited hardware. While contemporary fifth-generation (5G) systems offer substantial performance improvements over a diverse range of network evaluation metrics, they are still unable to fully meet the stringent energy and connectivity requirements of future IoT networks [2]–[4].

Despite the extensive research on the deployment of IoT networks, the issues of spectrum scarcity and limited energy reservoirs persist, particularly for systems employing orthogonal channel access methods, which are hindering their large-scale deployment. Moreover, owing to the costs incurred on their maintenance and sustained operation, conventional battery-powered options are not feasible for sustaining the long-term functionality of these IoT networks [5]. Consequently, energy harvesting techniques and wireless power transfer are actively investigated to enhance the manageability and independence of passive wireless sensors [6], [7]. Backscatter communication (BackCom) is known to be a promising energy-efficient solution for connecting a considerably large number of IoT devices in a cost-effective manner [8]–[10].

Through BackCom, passive backscatter nodes (BSNs) transmit their messages by modulating them over an incident carrier wave, or an ambient carrier, without the need for power-intensive radio-frequency (RF) chains. The information modulation is accomplished via impedance mismatch at the antenna terminals [9], [10]. In the traditional monostatic configuration, where the carrier emitter (CE) is co-located with the backscatter receiver (BR), the coverage range is restricted by the two-way path loss that the transmitted continuous-wave (CW) signal undergoes. Conversely, a bistatic configuration, where the CE and BR are spatially separated, can significantly extend the coverage range and allow for the ideal deployment of the CE to increase the efficiency of energy harvesting [11]. Recently, ambient BackCom, which exploits various ambient RF signals such as television, ZigBee, Wi-Fi, cellular, or LoRa, as opposed to traditional dedicated RF sources, is also under investigation to enable massive IoT networks due to its effective spectrum utilization and relatively low infrastructure cost [12].

M. Usman, S. Basharat, and S.A. Hassan are with the School of Electrical Engineering and Computer Science, National University of Sciences and Technology (NUST), Islamabad 44000, Pakistan. (e-mail: {musman.bee18seecs, sarah.phdee21seecs, ali.hassan}@seecs.edu.pk).

H. Pervaiz is with the School of Computer Science and Electronic Engineering, University of Essex, CO4 3SQ Colchester, U.K. (e-mail: haris.pervaiz@essex.ac.uk).

Z. Ding is with the Department of Electrical Engineering and Computer Science, Khalifa University, Abu Dhabi, UAE, and the Department of Electrical and Electronic Engineering, The University of Manchester, Manchester M13 9PL, U.K. (e-mail: zhiguo.ding@ku.ac.ae, zhiguo.ding@manchester.ac.uk).

H. Jung is with the Department of Electronic and Information Convergence Engineering, Kyung Hee University, Yongin, 17104, Korea. (e-mail: haejoonjung@khu.ac.kr).

The material in this paper was presented in part at IEEE International Conference on Distributed Computing Systems Workshops (ICDCSW), July 2022, Bologna, Italy [1].

This work was supported by Institute of Information & communications Technology Planning & evaluation (IITP) grant funded by the Korea government (MSIT) (No. RS-2024-00397480, System Development of Smart Repeater in Upper-mid Band).

This article has been accepted for publication in IEEE Transactions on Vehicular Technology. This is the author's version which has not been fully edited and content may change prior to final publication. Citation information: DOI 10.1109/TVT.2024.3440396



However, it is difficult to achieve stable performance, since the ambient signals are unpredictable and dynamic. Thus, it is critical to satisfy quality-of-service (QoS) even in dynamic wireless channel environments. To this end, reconfigurable intelligent surfaces (RISs) have been employed to realize the smart radio paradigm, as in [13]–[15].

RISs are planar surfaces that consist of a vast array of passive and low-cost elements, each with the capability to adjust both amplitude and phase of the incident radio signal. Thus, providing efficient control over the propagation characteristics of the wireless channel to achieve the desired channel response. Moreover, by optimally controlling the phases of the incident ray at a massive number of elements, significant beamforming gains can be achieved to boost the received signal strength (RSS), or reduce interference. RISs have drawn considerable research interest due to their scalable cost of deployment and ease of integration in the existing networks, and are anticipated to be an ideal candidate for enhancing the transmission range and capacity of the existing BackCom systems [16], [17]. In this regard, the authors in [18] investigated the transmit power minimization for the RIS-assisted bistatic BackCom system via a joint optimization of power reflection coefficients of BSNs, and active and passive beamforming vectors at the CE and RIS, respectively. Moreover, in [19], the authors studied the symbol error probability of the RIS-assisted BackCom system under coherent and random phase-shift schemes of the RIS.

Additionally, non-orthogonal multiple access (NOMA) is known to be an effective multiple-access technique to cater for the immense connectivity needs of IoT networks. In power-domain NOMA, multiple users are served on the same resource block by multiplexing their information in the power domain, as opposed to orthogonal resource (e.g., frequency, time, and code) allocation by the conventional orthogonal multiple access (OMA) variants. Thus, NOMA-enabled BackCom can significantly enhance the energy and spectral efficiency, and provide better user fairness [14], [20]. In this context, the authors in [21] demonstrated the effectiveness of the NOMA-enabled BackCom system, where the average number of successfully decoded bits was analyzed. Further, they presented the reflection coefficient selection criteria for the two-BSN pairing case. The authors in [22] considered the RIS-assisted bistatic NOMA-based BackCom system and maximized the sum rate by jointly optimizing the power reflection coefficients and RIS phase-shifts. In addition, [23] presented an iterative algorithm for the joint optimization of beamforming vectors, power allocation coefficients (PACs) at the transmitter, and RIS reflection coefficients for an RIS-assisted NOMA network. Moreover, the authors in [24] presented the design for the RIS-assisted BackCom system, and employed an efficient deep reinforcement learning algorithm to optimize both reflection coefficients and RIS phase shifts.

Inspired and motivated by the research contributions stated above, a multi-cluster NOMA-enabled RIS-assisted bistatic BackCom system is proposed in this work. The key contributions of this paper are summarized below.

- We present the cost-, energy-, and spectrum-efficient NOMA-enabled RIS-assisted bistatic BackCom system to support the massive IoT connectivity requirements of 6G systems. The proposed system supports the BSNs in the coverage area with multiple clusters, where each cluster employs NOMA to serve multiple BSNs, and an RIS to enhance the backscatter communication from the BSNs to the BR.
- We derive the closed-form expressions of BERs for two BSNs per cluster with coherent RIS phase-shift design and imperfect SIC, assuming the Nakagami-$m$ channel model. The derived results are verified by extensive simulations with various parameter configurations.
- We approximate the probability density function (PDF) of the sum of a Nakagami-$m$ and Gamma distribution by another Gamma distribution using the statistical method of moment matching.
- The improvement in effective non-erroneous bit transmissions by employing an RIS in the conventional BackCom system is investigated for different channel configurations and reflection coefficient pairs. The conventional NOMA-enabled BackCom system is notably outperformed by the proposed RIS-assisted system.

The remainder of this paper is structured as follows. Section II presents the system model and the transmission protocol for the multi-cluster NOMA-enabled RIS-assisted BackCom system. In Section III, we analyze the BER performance of 2-BSN NOMA cluster. It is followed by the analysis validation and performance evaluation in Section IV. Lastly, we provide the conclusions in Section V.

## II. System and Signal Model

We consider a multi-cluster bistatic BackCom network, as shown in Fig. 1, consisting of $N$ single-antenna backscatter nodes (BSNs), a single-antenna carrier emitter (CE), and a single-antenna backscatter receiver (BR)[1], with NOMA as the channel access method. The system is supplemented by an $M$-element RIS composed of a uniform planar array (UPA) of equally-spaced elements, where each passive reflecting element is capable of adjusting the phase of the impinging signal. Let the set of BSNs per cluster be represented by $\mathcal{J} = \{1, \ldots, J\}$, where $J = |\mathcal{J}|$ indicates the maximum permissible number of BSNs supported by a single cluster, with the minimum requirement being $J \geq 2$.

### A. BackCom Model

The sinusoidal CW signals are transmitted continuously by the CE, where each BSN modulates its information symbols onto the incident CW wave. The modulated signals are then received and decoded by the BR. The proposed model operates under two distinct transmission stages: (i) *excitation stage*, during which the CW broadcasting occurs; and (ii) *backscattering stage*, wherein the modulated signals are reflected by

[1]For analytical tractability and to simplify the statistical modeling of the RIS-aided backscatter channel, we consider a single antenna at the BR in this work, as in [5], [25]–[27]. The study of multi-antenna BR in an RIS-aided backscatter system is a promising direction for future work.

This article has been accepted for publication in IEEE Transactions on Vehicular Technology. This is the author's version which has not been fully edited and content may change prior to final publication. Citation information: DOI 10.1109/TVT.2024.3440396



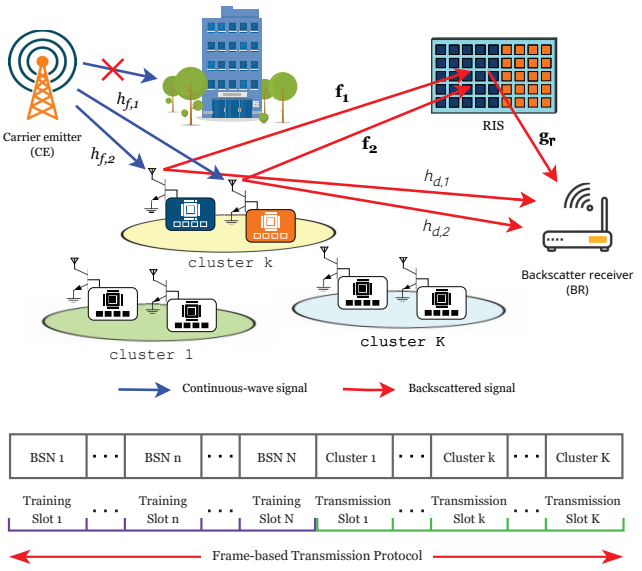


Fig. 1. An illustration of NOMA-enabled RIS-assisted bistatic BackCom system with $J = 2$.

the BSNs towards the BR via the RIS reflected and direct links. Given the substantial reduction in the RSS of the CW signal at the closely located RIS and BR, along with the absence of information embedding in the CW signal, we assume that there are no direct links from the CE to either the RIS or the BR [22], [28], [29].

*1) Modes of Operation:* In the proposed system, the BSNs have two distinct functioning modes, namely the waiting mode and the active mode. During the waiting mode, the BSNs stop backscattering and instead solely gather ambient energy from the incident CW signal. This energy is then stored in the battery to support sensing functionality and ensure continuous operation of the BSNs. In the active mode, the BSNs generate modulated backscatter by tuning their antenna impedance. Owing to the energy and complexity concerns of low-power BSNs, binary modulation schemes such as phase shift keying (PSK) and amplitude shift keying (ASK) are commonly adopted for BackCom systems [30]. Similarly, in this work, the binary phase-shift keying (BPSK) scheme is primarily considered for information transmission, wherein each BSN is equipped with two distinct impedance sets coupled with an RF transistor that enables the inbuilt microcontroller to generate two reflection coefficients for each impedance state, namely $\Gamma_1$ and $\Gamma_2$, where $\Gamma_1 > \Gamma_2$. Both reflection coefficients are of equal magnitude but differ in phase by 180°. Simulation results exhibiting BSNs' information transmission following quadrature phase-shift keying (QPSK) modulation are also provided to contrast the BER performance with respect to BPSK and to corroborate the performance analysis [31].

*2) Frame-based Transmission Protocol:* We consider a frame-based transmission protocol to integrate $J$-BSN NOMA pairing with the time-division multiple access (TDMA) protocol, as illustrated in Fig. 1. The proposed framework constitutes $N$ slots for the training phase, during which the RIS is inactive and the BR utilizes the channel state information (CSI) to distinguish between the strong and weak BSNs, and $K$ slots for the transmission phase. Moreover, as the processing delays arising from the SIC process and the associated hardware complexity increase with an increment in the supported BSNs per cluster, it is assumed that $J = 2$. For the training phase, a specific time slot is assigned to each BSN to reflect the CW signal towards the BR using the same reflection coefficient value, whereas all the other BSNs remain silent. The BR utilizes the estimated CSI acquired from the backscattered signals to sort the BSNs in order of decreasing signal strength, and accordingly, categorize the BSNs into two groups, namely the stronger BSNs and the weaker BSNs. Next, each stronger BSN is paired with a weaker BSN to form an ordered one-to-one mapping [32]. Only one cluster carries out the NOMA transmission in each transmission slot, wherein the strong and weak BSNs switch to their respective power reflection coefficients, i.e., $\Gamma_1$ and $\Gamma_2$, respectively.

## B. Signal Model

The $i$-th BSN's transmitted signal is given by

$$r_i = \sqrt{P_T \Gamma_i} h_{f,i} x_i, \tag{1}$$

where $r_i$ denotes the signal backscattered by the $i$-th BSN with the power reflection coefficient, $\Gamma_i$, and bearing the corresponding BPSK-modulated unit-power information symbol, $x_i$. $P_T$ denotes the transmit power of the CE. The forward channel coefficient, $h_{f,i}$, is assumed to be fading-free and determined by the path attenuation $L(d_{f,i})$, where $L(r) = r^{\gamma}$, $\gamma$ is the environment-specific path loss exponent, and $d_{f,i}$ denotes the distance from the CE to the $i$-th BSN. The assumption of a path loss-only channel model is reasonable in this context due to the strong line-of-sight (LoS) CE-BSN link owing to the deployment of BSNs in the immediate vicinity of the CE [33]. Furthermore, as the RIS is positioned near the BR, the reflected CW signal from the RIS towards the BSNs will experience a significant reduction in strength as a result of the multiplicative path attenuation along the reflected link. As a result, it can be regarded as insignificant. In each transmission slot, the signal received at the BR, $y$, is expressed as

$$y = \sum_{i=1}^{J} \sqrt{\Gamma_i P_T} h_{f,i} \left( \overbrace{\frac{h_{d,i}}{\sqrt{L(d_{d,i})}}}^{\text{direct link}} + \overbrace{\frac{\mathbf{g}_r^{\mathrm{H}} \boldsymbol{\Theta} \mathbf{f}_i}{\sqrt{L(d_{b,i}) L(d_I)}}}^{\text{RIS reflected link}} \right) x_i + w, \tag{2}$$

where $d_{d,i}$ and $h_{d,i}$ represent the distance from the BR to the $i$-th BSN, and the direct-link channel coefficient, respectively. Likewise, the distances from the RIS to the CE and the $i$-th BSN are denoted by $d_I$ and $d_{b,i}$, respectively. $\mathbf{f}_i \in \mathbb{C}^{M \times 1}$ denotes the small-scale fading coefficient vector between the RIS and the $i$-th BSN, and $\mathbf{g}_r \in \mathbb{C}^{M \times 1}$ is the fading vector of the RIS-BR link. In this work, we adopt the quasi-static flat-fading channel model, whereby the channel characteristics for each BSN remain relatively constant during a single transmission frame, but vary from frame to frame. Further, $w$ is the zero-mean additive white Gaussian noise represented by $w \sim \mathcal{CN}(0, \sigma^2)$, where $\sigma^2$ is the variance. The diagonal matrix, $\boldsymbol{\Theta} \in \mathbb{C}^{M \times M}$,

is defined as $\mathbf{\Theta} = \text{diag}\left(\beta_1 e^{j\theta_1}, \beta_2 e^{j\theta_2} \dots \beta_M e^{j\theta_M}\right)$, where $\theta_m \in \Phi$ is the induced phase-shift at the $m$-th RIS element, and $\beta_m \in [0,1]$[2] is the amplitude reflection coefficient. We consider the coherent phase-shift design in this work, where $\theta_m \in [0, 2\pi)$ and $\Phi$ denotes the set of *continuous phase-shifts* [34].

RIS optimization necessitates the availability of CSI for both BSNs-RIS and RIS-BR links. As RISs do not employ any RF chains and due to inherent coupling between the reflection coefficient matrix at the RIS and the BSNs-RIS and RIS-BR channels, only the cascaded BSNs-RIS-BR channel is estimated at the BR, which is sufficient in most cases. In this work, it is assumed that the CSI of the cascaded channel has been obtained via state-of-the-art channel estimation methods such as binary and full reflection-based direct cascaded channel estimation (DCCE) [35], subspace-based estimation methods [36], and compressed sensing (CS)-based channel estimation [37].

We assume that each RIS element reflects the incident signals independently, thereby eliminating any signal coupling between adjacent elements during reflection. Therefore, the RIS reflected link is expressed equivalently as

$$\mathbf{g}_r^H \mathbf{\Theta} \mathbf{f}_i = \sum_{m=1}^{M} e^{j\theta_m} f_{i,m}\, g_{r,m}, \tag{3}$$

where $f_{i,m}$ and $g_{r,m}$ are the $m$-th elements of $\mathbf{f}_i$ and $\mathbf{g}_r^H$, respectively. This work adopts the surface partitioning, as in [20], wherein the elements in the RIS are divided amongst the $J$ BSNs. The split factor, i.e., $\alpha \in [0,1]$, specifies the distribution of these elements, and is defined as

$$\alpha = \frac{M_1}{M}, \tag{4}$$

where $M_1$ represents the number of RIS elements, rounded up to the next natural number, allocated to BSN-1 for improving its performance via the coherent combination of RIS reflected and direct signals at the BR. Conversely, the remaining elements, i.e., $M_2 = M - M_1$, are configured for BSN-2. Furthermore, for coherently optimized RIS elements, the phase shifts are chosen as $\theta_m = \angle h_{d,i} - \angle\left(f_{i,m}\, g_{r,m}\right)$ [38]. The resultant RIS reflected link can be expressed as

$$\sum_{m \in E_i} e^{j\theta_m} f_{i,m}\, g_{r,m} = \sum_{m \in E_i} e^{j\angle h_{d,i}} \left|f_{i,m}\right| \left|g_{r,m}\right|, \tag{5}$$

where the set $E_i$ denotes the elements allocated to the $i$-th BSN.

### C. SIC-based Information Decoding

The BR adopts the successive interference cancellation (SIC) algorithm to segregate and decode the BSNs' transmitted signals. The transmit SNR compensates for the path-loss attenuation effect of the forward channels, $h_{f,1}$ and $h_{f,2}$. Hence, they are excluded from the subsequent analysis. For the case $J = 2$, it is considered, without loss of generality, that BSN-1 has a greater channel gain compared to BSN-2, i.e., $\left|h_{b,1}\right|^2 > \left|h_{b,2}\right|^2$, where $h_{b,i} = \frac{h_{d,i}}{\sqrt{L(d_{d,i})}} + \frac{\mathbf{g}_r^H \mathbf{\Theta} \mathbf{f}_i}{\sqrt{L(d_{b,i}) L(d_I)}}$ is the $i$-th BSN's backward channel. Under this scheme, the information symbol of the stronger BSN (i.e., BSN-1) is decoded first by the BR, which is then deducted from the composite received signal in order to recover the information of the weaker BSN (i.e., BSN-2). Thus, the sequence for decoding follows a descending order of channel gains.

The BR employs maximum-likelihood detection (MLD) for BSN-1's signal decoding while treating the constituent signal of BSN-2 as inter-user interference (IUI). Assuming perfect CSI at the BR, the detection for BSN-1's symbol is expressed as [39]

$$\hat{x}_1 = \underset{\tilde{x}_1 \in S}{\arg\min} \left| y - \sqrt{\Gamma_1 P_T} h_{b,1} \tilde{x}_1 \right|^2, \tag{6}$$

where $\hat{x}_1$ is the estimated data symbol of BSN-1 and $\tilde{x}_1$ indicates the possible trial value of $x_1$, which belongs to $S = \{-1, +1\}$, the set of all feasible signal space points. If the BR successfully detects $x_1$, an IUI-free decoding for BSN-2's symbol is carried out. However, an incorrect BSN-1 detection induces a bit error, which causes an error propagation (i.e., IUI) for BSN-2's symbol detection. Thus, for BSN-2, the MLD is expressed as

$$\hat{x}_2 = \underset{\tilde{x}_2 \in S}{\arg\min} \left| (y - \sqrt{\Gamma_1 P_T} h_{b,1} \hat{x}_1) - \sqrt{\Gamma_2 P_T} h_{b,2} \tilde{x}_2 \right|^2, \tag{7}$$

where $\tilde{x}_2$ and $\hat{x}_2$ denote the possible trial value of $x_2$ and the estimated data symbol of BSN-2, respectively. An error occurs when $\hat{x}_2 \neq x_2$.

## III. Bit Error Rate Analysis

Now, we analyze the average error probability for the two BSNs and derive the closed-form expressions. Since the signal received by the BR is the sum of both BSNs' signals, the resultant received symbol is the superposition of individual BSNs' BPSK symbols, which corresponds to four constellation points in total. Fig. 2 depicts the resulting signal space of the proposed system.

In the figure, the blue diamonds refer to the originally transmitted information bits of BSN-1, corresponding to BPSK symbol $x_1$, and its distance from the decision boundary is subject to the received signal power of BSN-1 signal, $u_1$, whereas the red circles indicate the translated BSN-1 bits due to the IUI from BSN-2. $u_2$ corresponds to BSN-2's signal. The constellation points are represented by the pair $(b_1, b_2)$, where $b_1$ and $b_2$ are the BPSK bits of BSN-1 and BSN-2, respectively. The system performance is subject to the selected values of the reflection coefficients, i.e., to the position of the constellation points, which changes the respective distance from the decision boundary.

### A. BER of BSN-1

The detection of BSN-1 signal is carried out according to (6), wherein the SIC process is not required. An error occurs

[2]It is assumed that the incident signal's amplitude remains unaffected by the RIS. Therefore, in the subsequent sections, we assume $\beta_1 = \beta_2 = \dots = \beta_M = 1$.

This article has been accepted for publication in IEEE Transactions on Vehicular Technology. This is the author's version which has not been fully edited and content may change prior to final publication. Citation information: DOI 10.1109/TVT.2024.3440396



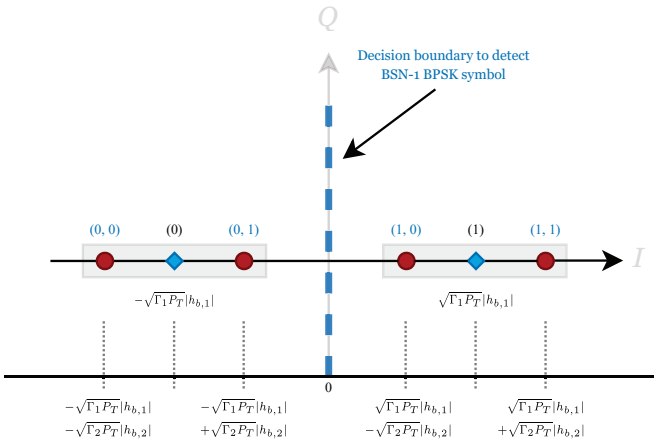


Fig. 2. The signal constellation diagram for the received symbols at the BR.

when $\hat{x}_1 \neq x_1$, and the probability of such error, denoted by $P_e(u_1)$, can be derived as follows. Because of interference, there are four possible cases in which BSN-1 bits can be decoded erroneously.

For the constellation point $(0,0)$, i.e., when both BSNs transmit bit '0', the decision boundary is $\sqrt{\Gamma_2 P_T}|h_{b,2}| + \sqrt{\Gamma_1 P_T}|h_{b,1}|$ away from the specified point, thus, an error occurs when the in-phase (I) component of $w$, denoted by $n$, exceeds this distance, which can be mathematically expressed as

$$n \geq \sqrt{\Gamma_2 P_T}|h_{b,2}| + \sqrt{\Gamma_1 P_T}|h_{b,1}|. \tag{8}$$

For the constellation point $(0,1)$, i.e., when BSN-1 transmits bit '0' and BSN-2 transmits bit '1', an error occurs when the following condition is satisfied.

$$n \geq \sqrt{\Gamma_1 P_T}|h_{b,1}| - \sqrt{\Gamma_2 P_T}|h_{b,2}|. \tag{9}$$

Likewise, following the same procedure for each symbol, the corresponding error is calculated and multiplied by the prior probability. Considering equiprobable symbols and the signal space symmetry, the probability of error $P_e(u_1)$ can be expressed as

$$P_e(u_1) = \frac{1}{2}[\mathbb{P}(n \geq \mathcal{H}_1 + \mathcal{H}_2) + \mathbb{P}(n \geq \mathcal{H}_1 - \mathcal{H}_2)], \tag{10}$$

where $\mathcal{H}_i = \sqrt{\Gamma_i P_T}|h_{b,i}|$ and $\mathbb{P}(A)$ represents the probability of event $A$. Since $n \sim \mathcal{N}(0, \sigma^2/2)$, $P_e(u_1)$ can equivalently be expressed in terms of the $\mathcal{Q}$-function as

$$P_e(u_1) = \frac{1}{2}[\mathcal{Q}(\mathcal{U}) + \mathcal{Q}(\mathcal{V})], \tag{11}$$

where

$$\mathcal{U} = \frac{\mathcal{H}_1 + \mathcal{H}_2}{\sqrt{\sigma^2/2}}, \tag{12}$$

and

$$\mathcal{V} = \frac{\mathcal{H}_1 - \mathcal{H}_2}{\sqrt{\sigma^2/2}}. \tag{13}$$

The evaluation of the average error probability requires the computation of an integral, whose integrand is the product of a Gaussian $\mathcal{Q}$-function, with an argument proportional to the instantaneous SNR of the received signal, and the fading distribution of the propagation channel [40]. Hence, BSN-1's average BER, represented by $\overline{P_e(u_1)}$, is computed by averaging with respect to the two random variables (RVs) $\mathcal{U}$ and $\mathcal{V}$. Let $f_{\mathcal{U}}(u)$ and $f_{\mathcal{V}}(v)$ be the PDFs of $\mathcal{U}$ and $\mathcal{V}$, respectively. It is noted that the two RVs correspond to the sum and difference of the backward channels, $\mathcal{H}_1$ and $\mathcal{H}_2$, which are subject to fading. Hence, the average error probability of BSN-1 is given by

$$\overline{P_e(u_1)} = \frac{1}{2}\Big[\int_{-\infty}^{+\infty} \mathcal{Q}(\mathcal{U}) f_{\mathcal{U}}(u)\,\mathrm{d}u + \int_{-\infty}^{+\infty} \mathcal{Q}(\mathcal{V}) f_{\mathcal{V}}(v)\,\mathrm{d}v\Big]. \tag{14}$$

In order to compute the PDFs of the RVs $\mathcal{U}$ and $\mathcal{V}$, we first determine the distribution of $\mathcal{H}_i$, which is the sum of a scaled Nakagami-$m$ RV with PDF given as

$$f(x; m, \Omega) = \frac{2m^m}{\Gamma(m)\Omega^m} x^{2m-1} \exp\Big(-\frac{m}{\Omega}x^2\Big), \forall\, x \geq 0, \tag{15}$$

where $m \geq \frac{1}{2}$ and $\Omega > 0$ are the shape and spread parameters, respectively, and the distribution of the RIS reflected link. Following Lemmas 2 and 3 in [41], $\left|\mathbf{g}_r^H \mathbf{\Theta} \mathbf{f}_i\right|$ can be approximated by the Gamma distribution as

$$\left|\mathbf{g}_r^H \mathbf{\Theta} \mathbf{f}_i\right| \sim \Gamma\Big(M_i \frac{\mu_i^2}{1-\mu_i^2}, \frac{1-\mu_i^2}{\mu_i}\Big), \tag{16}$$

with

$$\mu_i = \frac{\Gamma(m_{f_i} + \frac{1}{2}) \times \Gamma(m_{g_r} + \frac{1}{2})}{\Gamma(m_{f_i}) \times \Gamma(m_{g_r}) \times (m_{f_i} m_{g_r})^{1/2}}, \tag{17}$$

where $\Gamma(.,.)$ represents a Gamma-distributed RV, whereas $\Gamma(.)$ denotes the gamma function. $M_i$ refers to the number of RIS elements configured for the $i$-th BSN. Moreover, a Gamma RV $X \sim \Gamma(k, \theta)$, where $\theta$ and $k$ are the scale and shape parameters, respectively, has the following PDF

$$f(x; k, \theta) = \frac{x^{k-1}}{\theta^k} \frac{e^{-x/\theta}}{\Gamma(k)}, \tag{18}$$

where $x > 0$ with positive $k$ and $\theta$. Using the scaling properties of the Nakagami-$m$ and Gamma distributions, the direct and RIS-reflected links are distributed as

$$\frac{|h_{d,i}|}{\sqrt{L(d_{d,i})}} \sim \textit{Nakagami}\Big(m_{h_{d,i}}, \frac{1}{L(d_{d,i})}\Big), \tag{19}$$

and

$$\frac{\left|\mathbf{g}_r^H \mathbf{\Theta} \mathbf{f}_i\right|}{\sqrt{L(d_{b,i})L(d_I)}} \sim \Gamma\Big(M_i \frac{\mu_i^2}{1-\mu_i^2}, \frac{1-\mu_i^2}{\mu_i \sqrt{L(d_{b,i})L(d_I)}}\Big). \tag{20}$$

Thus, $\mathcal{H}_i$ is essentially the sum of a Nakagami-distributed RV and a Gamma-distributed RV, whose PDF can be obtained by convolving the PDFs of the two individual distributions, provided they are independent. However, in the following lemma, we use the method of moments (MoM) to approximate $\mathcal{H}_i$ by another Gamma-distributed RV.

*Lemma 1:* We can approximate the distribution of the sum of a Nakagami-$m$ RV, $Y_1$, with parameters $m_1$ and $\Omega_1$, and a Gamma RV, $Y_2$, with parameters $k_2$ and $\theta_2$, by another Gamma

This article has been accepted for publication in IEEE Transactions on Vehicular Technology. This is the author's version which has not been fully edited and content may change prior to final publication. Citation information: DOI 10.1109/TVT.2024.3440396



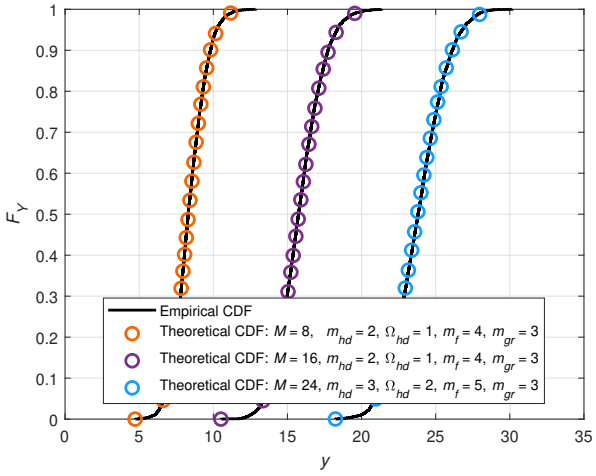


Fig. 3. Comparison of the empirical and theoretical CDFs with MoM for the sum of Nakagami-$m$ and Gamma distributions.

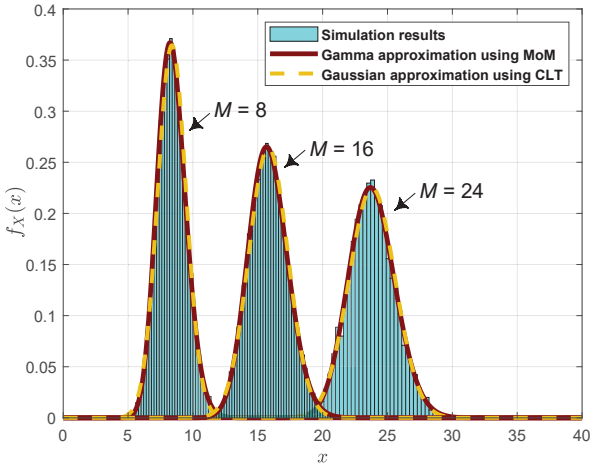


Fig. 4. Comparison of empirical PDF, theoretical PDF obtained using MoM, and CLT-based Gaussian approximation for the sum of Nakagami-$m$ and Gamma distributions.

RV, $\mathcal{S}$. In other words, $\mathcal{S} = Y_1 + Y_2$ with parameters $k_s$ and $\theta_s$ follows the PDF as

$$f(s; k_s, \theta_s) = \frac{s^{k_s-1} e^{-s/\theta_s}}{\theta_s^{k_s}\,\Gamma(k_s)}, \forall\, s > 0 \text{ and } k_s, \theta_s > 0, \quad (21)$$

where

$$k_s = \frac{\mathbb{E}[\mathcal{S}]^2}{\mathbb{V}[\mathcal{S}]} = \frac{\mathbb{E}[\mathcal{S}]^2}{\mathbb{E}[\mathcal{S}^2] - \big(\mathbb{E}[\mathcal{S}]\big)^2}, \quad (22)$$

and

$$\theta_s = \frac{\mathbb{V}[\mathcal{S}]}{\mathbb{E}[\mathcal{S}]} = \frac{\mathbb{E}[\mathcal{S}^2] - \big(\mathbb{E}[\mathcal{S}]\big)^2}{\mathbb{E}[\mathcal{S}]}, \quad (23)$$

where $\mathbb{E}[.]$ corresponds to the statistical average and $\mathbb{V}[.]$ represents the variance.

*Proof.* A two-step proof is required to estimate the sum of $Y_1$ and $Y_2$ by another Gamma RV, $\mathcal{S}$. First, the MoM is used to match the first two moments of $Y = Y_1 + Y_2$ with the first two moments of $\mathcal{S}$. Further, the $p$-th moment of Nakagami-$m$ RV $Y_1$ is expressed as

$$\mathbb{E}[Y_1^p] = \frac{\Gamma(m_1 + \frac{p}{2})}{\Gamma(m_1)} \Big(\frac{\Omega_1}{m_1}\Big)^{p/2}, \quad (24)$$

whereas the $p$-th moment of Gamma RV $Y_2$ is

$$\mathbb{E}[Y_2^p] = \theta_2^p \frac{\Gamma(p + k_2)}{\Gamma(k_2)}. \quad (25)$$

By the multinomial theorem and assuming that $Y_1$ and $Y_2$ are independent, the first moment of $Y$ is matched with that of the RV $\mathcal{S}$, i.e.,

$$\begin{aligned}\mathbb{E}[\mathcal{S}] &= \mathbb{E}[Y] = \mathbb{E}[Y_1] + \mathbb{E}[Y_2] \\ &= \frac{\Gamma(m_1 + \frac{1}{2})}{\Gamma(m_1)} \Big(\frac{\Omega_1}{m_1}\Big)^{1/2} + k_2\,\theta_2. \end{aligned} \quad (26)$$

Again using the multinomial theorem to match the second moments of the two RVs, $\mathbb{E}[\mathcal{S}^2]$ is calculated as

$$\begin{aligned}\mathbb{E}[\mathcal{S}^2] &= \mathbb{E}[Y^2] = \mathbb{E}[{Y_1}^2] + \mathbb{E}[{Y_2}^2] + 2 \cdot \mathbb{E}[Y_1]\,\mathbb{E}[Y_2] \\ &= \Omega_1 + \theta_2^2\,(k_2 + k_2^2) + 2 \cdot \frac{k_2\,\theta_2\,\Gamma(m_1 + \frac{1}{2})}{\Gamma(m_1)} \Big(\frac{\Omega_1}{m_1}\Big)^{1/2}. \end{aligned} \quad (27)$$

Then, by using (22) and (23), the values of $k_s$ and $\theta_s$ can be readily determined.

Kolmogorov–Smirnov (K-S) test (see Appendix) is conducted, in the second step, for the sum of Nakagami-$m$ and Gamma RV, modeling the direct and RIS-reflected channel, respectively. In Fig. 3, the estimated theoretical and empirical cumulative distribution functions (CDFs) of the summation of the Nakagami-$m$ and Gamma RV are plotted. We observe that the estimated theoretical CDFs are in line with the empirical CDFs, establishing that the Gamma RV, $S$, can indeed approximate the distribution of $Y$. Whereas, Fig. 4 compares the PDF of the combined backscatter channel obtained using the numerical simulations with the Gamma distribution derived in Sec. III-A, and the CLT-based Gaussian approximation given in (31). The characteristic parameters of both distributions are varied to simulate different conditions. □

Finally, $\mathcal{H}_i$ can be approximated as

$$\mathcal{H}_i \sim \Gamma(k_{\mathcal{H}_i}, \theta_{\mathcal{H}_i}), \quad (30)$$

where $k_{\mathcal{H}_i}$ and $\theta_{\mathcal{H}_i}$ are the parameters matched by MoM, as in *Lemma 1*. Furthermore, for sufficiently large values of $k_{\mathcal{H}_i}$, the central limit theorem (CLT) can be invoked to realize a Normal approximation to the distribution of $\mathcal{H}_i$, having the mean and variance of $k_{\mathcal{H}_i}\theta_{\mathcal{H}_i}$ and $k_{\mathcal{H}_i}\theta_{\mathcal{H}_i}^2$, respectively, i.e.,

$$\mathcal{H}_i \sim \mathcal{N}(k_{\mathcal{H}_i}\theta_{\mathcal{H}_i}, k_{\mathcal{H}_i}\theta_{\mathcal{H}_i}^2). \quad (31)$$

Therefore, $\mathcal{U}$ and $\mathcal{V}$ are essentially the sum and difference, respectively, of the two independent Gaussian RVs, and their corresponding PDFs are

$$f_{\mathcal{U}}(u) = \mathcal{N}(\mu_{\mathcal{U}}, \sigma_{\mathcal{U}}^2), \quad (32)$$

and

$$f_{\mathcal{V}}(v) = \mathcal{N}(\mu_{\mathcal{V}}, \sigma_{\mathcal{V}}^2), \quad (33)$$

$$P_e^I(u_2) = \frac{1}{2}[\mathbb{P}(n \leq \mathcal{H}_1 + \mathcal{H}_2) \cdot \mathbb{P}(n \geq \mathcal{H}_2 \mid n \leq \mathcal{H}_1 + \mathcal{H}_2) + \mathbb{P}(n \leq \mathcal{H}_1 - \mathcal{H}_2) \cdot \mathbb{P}(n \leq -\mathcal{H}_2 \mid n \leq \mathcal{H}_1 - \mathcal{H}_2)]. \quad (28)$$

$$P_e^{II}(u_2) = \frac{1}{2}[\mathbb{P}(n \geq \mathcal{H}_1 + \mathcal{H}_2) \cdot \mathbb{P}(n \geq 2 \cdot \mathcal{H}_1 + \mathcal{H}_2 \mid n \geq \mathcal{H}_1 + \mathcal{H}_2) + \mathbb{P}(n \geq \mathcal{H}_1 - \mathcal{H}_2) \cdot \mathbb{P}(n \leq 2 \cdot \mathcal{H}_1 - \mathcal{H}_2 \mid n \geq \mathcal{H}_1 - \mathcal{H}_2)]. \quad (29)$$

where

$$\mu_{\mathcal{U}} = \frac{k_{\mathcal{H}_1}\theta_{\mathcal{H}_1} + k_{\mathcal{H}_2}\theta_{\mathcal{H}_2}}{\sqrt{\sigma^2/2}},$$
$$\mu_{\mathcal{V}} = \frac{k_{\mathcal{H}_1}\theta_{\mathcal{H}_1} - k_{\mathcal{H}_2}\theta_{\mathcal{H}_2}}{\sqrt{\sigma^2/2}},$$

and

$$\sigma_{\mathcal{U}}^2 = \sigma_{\mathcal{V}}^2 = \frac{k_{\mathcal{H}_1}\theta_{\mathcal{H}_1}^2 + k_{\mathcal{H}_2}\theta_{\mathcal{H}_2}^2}{\sigma^2/2}.$$

Thus, (14) involves the integration of the product of a Gaussian distribution and the $\mathcal{Q}$-function, the closed-form of which is derived in [5], and is given as

$$\int_{-\infty}^{+\infty} \mathcal{Q}(\mathcal{Z}) f_{\mathcal{Z}}(z)\, \mathrm{d}z = \Lambda(\mu_Z, \sigma_Z^2) = \mathcal{Q}\Big(\frac{\mu_Z}{\sqrt{\sigma_Z^2 + 1}}\Big), \quad (34)$$

where $\mathcal{Z} \sim \mathcal{N}(\mu_Z, \sigma_Z^2)$. Therefore, the average probability of error for $u_1$ is

$$\overline{P_e(u_1)} = \frac{1}{2}(\Lambda(\mu_{\mathcal{U}},\, \sigma_{\mathcal{U}}^2) + \Lambda(\mu_{\mathcal{V}},\, \sigma_{\mathcal{V}}^2)). \quad (35)$$

### *B. BER of BSN-2*

The detection of BSN-2's signal is carried out through the SIC decoding process, whereby the BR first decodes BSN-1 bit according to (6), and then decodes BSN-2 bit after deducting the recovered BSN-1 symbol, $\hat{x}_1$, from the composite signal $y$. Accordingly, the detected $\hat{x}_2$ can be stated as

$$\hat{x}_2 = \underset{\tilde{x}_2 \in S}{\arg\min} \left| y_{SIC} - \sqrt{\Gamma_2 P_T} h_{b,2} \tilde{x}_2 \right|^2, \quad (36)$$

where $y_{SIC}$ corresponds to the resultant signal at the BR after the SIC process. Therefore, if BR decodes $u_1$ correctly, then $y_{SIC} = \sqrt{\Gamma_2 P_T} h_{b,2} x_2 + w$ which results in an IUI-free decoding. However, in the case of incorrect decoding of $u_1$, i.e., $\hat{x}_1 \neq x_1$, $y_{SIC} = \sqrt{\Gamma_1 P_T} h_{b,1} x_1 - \sqrt{\Gamma_1 P_T} h_{b,1} \hat{x}_1 + \sqrt{\Gamma_2 P_T} h_{b,2} x_2 + w$, and the decoding process of BSN-2 is influenced by the reconstructed BSN-1 bit, $\hat{x}_1$. An error occurs when $\hat{x}_2 \neq x_2$, and the corresponding error probability is given by $P_e(u_2)$. Since the SIC process could result either in a correct detection of BSN-1 bit or an erroneous detection, the error probability of BSN-2 is analyzed under two cases.

*1) Case I: Correct detection of BSN-1 bit by the BR:* We first consider the case when BSN-1 bit is decoded correctly by the BR. For the constellation points $(0, 0)$ and $(1, 1)$, the prior probability, i.e., the probability of BSN-1 symbol being decoded correctly, is $\frac{1}{4} \times \mathbb{P}(n \leq \mathcal{H}_1 + \mathcal{H}_2)$, which is the complement of the event described in (8) that gives the error probability of BSN-1 bit. Moreover, the decision boundary for $x_2$'s detection, as determined by the SIC decoding outcome, impacts the error probability of BSN-2 bit.

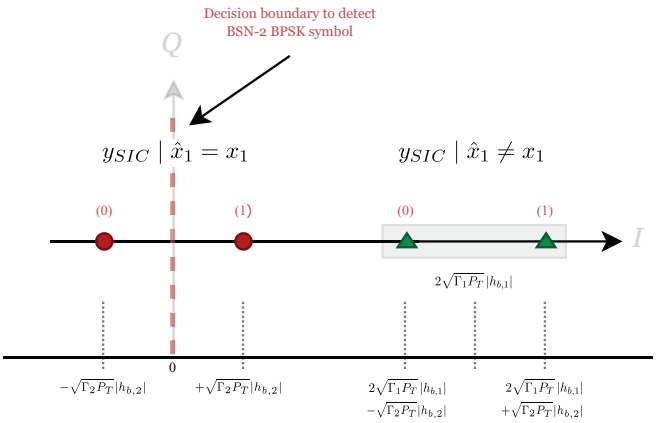


Fig. 5. The signal constellation diagram of BSN-2's received symbols for $b_1 = 1$ with $y_{SIC} \mid_{\hat{x}_1 = x_1}$ and $y_{SIC} \mid_{\hat{x}_1 \neq x_1}$.

For the constellation point $(0, 0)$ with correct detection of $u_1$, $y_{SIC}$ reduces to $-\sqrt{\Gamma_2 P_T} h_{b,2} + w$, and the condition for incorrect BSN-2 bit detection can be inferred from Fig. 5, which is given by

$$n \geq \sqrt{\Gamma_2 P_T} \left| h_{b,2} \right|, \quad (37)$$

and for the constellation point $(1, 1)$ with correct detection of $u_1$, the error condition for BSN-2 bit is

$$n \leq -\sqrt{\Gamma_2 P_T} \left| h_{b,2} \right|. \quad (38)$$

Similarly, following the same procedure for the remaining constellation points, $(0, 1)$ and $(1, 0)$, the error probability for BSN-2 bit with correct $u_1$ decoding is given by (28). Moreover, by using the law of conditional probability, $P_e^I(u_2)$ can be stated as

$$P_e^I(u_2) = \frac{1}{2}[\mathbb{P}(n \geq \mathcal{H}_2) \cdot \mathbb{P}(\mathcal{H}_2 \leq n \leq \mathcal{H}_1 + \mathcal{H}_2)], \quad (39)$$

which can equivalently be represented by considering the distribution of $n$ as

$$P_e(u_1) = \mathcal{Q}(\mathcal{X}) - \frac{1}{2}\mathcal{Q}(\mathcal{U}), \quad (40)$$

where $\mathcal{U}$ is defined in (12) and

$$\mathcal{X} = \frac{\mathcal{H}_2}{\sqrt{\sigma^2/2}}. \quad (41)$$

*2) Case II: Incorrect detection of BSN-1 bit by the BR:* In the case when BSN-1 symbol is incorrectly decoded by the BR, the error propagation from SIC process will influence the decision boundary for BSN-2 as well. The probability of $u_1$ in error is given by (10), and will function as the prior probability for this case. Following the same procedure described in Case

This article has been accepted for publication in IEEE Transactions on Vehicular Technology. This is the author's version which has not been fully edited and content may change prior to final publication. Citation information: DOI 10.1109/TVT.2024.3440396



$I$, the error probability for BSN-2 signal with incorrect $u_1$ decoding is given by (29). However, IUI from BSN-1 results in an error propagation of $2 \cdot \mathcal{H}_1$ during the detection of $x_2$. This can be inferred from the expression for $y_{SIC}$ given in Sec. III-B for the case of incorrect decoding, and from the translated signal points indicated by green triangles in Fig. 5.

Moreover, by invoking the law of conditional probability, the expression in (29) can equivalently be stated as

$$P_e^{II}(u_2) = \frac{1}{2}[\mathbb{P}(n \geq 2 \cdot \mathcal{H}_1 + \mathcal{H}_2) + \mathbb{P}(\mathcal{H}_1 - \mathcal{H}_2 \leq n \leq 2 \cdot \mathcal{H}_1 - \mathcal{H}_1], \quad (42)$$

and in terms of $\mathcal{Q}$-function notation as

$$P_e^{II}(u_2) = \frac{1}{2}[\mathcal{Q}(\mathcal{W}) + \mathcal{Q}(\mathcal{V}) - \mathcal{Q}(\mathcal{Y})], \quad (43)$$

where $\mathcal{V}$ is given by (13), whereas the RVs $\mathcal{W}$ and $\mathcal{Y}$ are defined as

$$\mathcal{W} = \frac{2 \cdot \mathcal{H}_1 + \mathcal{H}_2}{\sqrt{\sigma^2/2}}, \quad (44)$$

and

$$\mathcal{Y} = \frac{2 \cdot \mathcal{H}_1 - \mathcal{H}_2}{\sqrt{\sigma^2/2}}. \quad (45)$$

Hence, for $u_2$, the total probability of error can be obtained as the sum of both cases, in (40) and (43), and is expressed as

$$P_e(u_2) = P_e^{I}(u_2) + P_e^{II}(u_2). \quad (46)$$

Finally, using (40) and (43), we get

$$P_e(u_2) = \mathcal{Q}(\mathcal{X}) + \frac{1}{2}[-\mathcal{Q}(\mathcal{U}) + \mathcal{Q}(\mathcal{V}) + \mathcal{Q}(\mathcal{W}) - \mathcal{Q}(\mathcal{Y})]. \quad (47)$$

Since the BER expression for $u_2$ contains $\mathcal{Q}$-functions of RVs whose PDFs can also be approximated by a scaled Normal distribution, the average BER, $\overline{P_e(u_2)}$, for BSN-2 is evaluated similarly to $\overline{P_e(u_1)}$, and is given by

$$\overline{P_e(u_2)} = \Lambda(\mu_{\mathcal{X}}, \sigma_{\mathcal{X}}^2) + \frac{1}{2}[-\Lambda(\mu_{\mathcal{U}}, \sigma_{\mathcal{U}}^2) + \Lambda(\mu_{\mathcal{V}}, \sigma_{\mathcal{V}}^2) + \Lambda(\mu_{\mathcal{W}}, \sigma_{\mathcal{W}}^2) - \Lambda(\mu_{\mathcal{Y}}, \sigma_{\mathcal{Y}}^2)], \quad (48)$$

where

$$\mu_{\mathcal{X}} = \frac{k_{\mathcal{H}_2}\theta_{\mathcal{H}_2}}{\sqrt{\sigma^2/2}}, \; \sigma_{\mathcal{X}}^2 = \frac{k_{\mathcal{H}_2}\theta_{\mathcal{H}_2}^2}{\sigma^2/2},$$
$$\mu_{\mathcal{W}} = \frac{2 \cdot k_{\mathcal{H}_1}\theta_{\mathcal{H}_1} + k_{\mathcal{H}_2}\theta_{\mathcal{H}_2}}{\sqrt{\sigma^2/2}},$$
$$\mu_{\mathcal{Y}} = \frac{2 \cdot k_{\mathcal{H}_1}\theta_{\mathcal{H}_1} - k_{\mathcal{H}_2}\theta_{\mathcal{H}_2}}{\sqrt{\sigma^2/2}},$$

and

$$\sigma_{\mathcal{W}}^2 = \sigma_{\mathcal{Y}}^2 = \frac{4 \cdot k_{\mathcal{H}_1}\theta_{\mathcal{H}_1}^2 + k_{\mathcal{H}_2}\theta_{\mathcal{H}_2}^2}{\sigma^2/2}.$$

TABLE I
EXECUTION TIMES FOR SIMULATION-BASED BER RESULTS

| System | Average Running Time (s) | |
|---|---|---|
| | $M = 24, I_o = 10^5$ | $M = 42, I_o = 10^6$ |
| RIS-NOMA-BackCom | 83.13 | 1454.86 |
| RIS-OMA-BackCom | 46.27 | 554.85 |

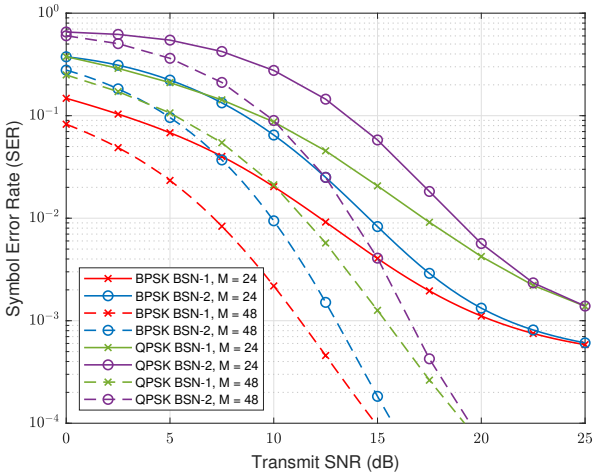


Fig. 6. SER performance evaluation of BSN-1 and BSN-2 employing BPSK and QPSK modulations with $\alpha = 0.6$.

## IV. NUMERICAL RESULTS AND PERFORMANCE ANALYSIS

In this section, we present the simulation results to validate the BER expressions derived in the preceding section and provide important insights into the performance of the proposed system. In particular, we provide the BER performance of both BSNs for various parameter configurations, demonstrating the superior performance of the RIS-NOMA-BackCom system over benchmark schemes, including OMA-BackCom, NOMA-BackCom, and RIS-OMA-BackCom. The curves obtained from the analytical derivations are matched with Monte Carlo simulation runs, denoted by $I_o$, tailored to meet the numerical bounds dictated by the minimum BER value. Simulations are conducted on a computer equipped with a 13th Gen Intel® Core™ i5-13600K 3.5GHz CPU and 32GB RAM, complemented by an NVIDIA GeForce RTX 3070 GPU. The execution times for simulation-based BER results, obtained through a sweep over the SNR values, are provided in Table I. The large-scale path loss model employed for the composite backscatter channel is given in Sec. II-B. As in [22], we consider a two-dimensional network, where the CE, BR, and RIS are positioned at the origin, $(70, 0)$ meters, and $(50, 0)$ meters, respectively. The BSNs are symmetrically distributed at a distance of 25 meters from the CE. Additionally, suitable split factor value and reflection coefficients, i.e., $\Gamma_1$ and $\Gamma_2$ [3], are considered in order to ensure successful decoding at the

[3]Backscatter nodes need to harvest a certain amount of energy from the incident CW signal to power their circuitry and thus have a much smaller power reflection coefficient in practice.

This article has been accepted for publication in IEEE Transactions on Vehicular Technology. This is the author's version which has not been fully edited and content may change prior to final publication. Citation information: DOI 10.1109/TVT.2024.3440396



BR. Unless stated otherwise, the simulation parameters are specified in Table II.

TABLE II
SIMULATION PARAMETERS

| Parameters | Values |
|---|---|
| Transmit power | $P_T$ = 30 dBm |
| Path loss exponent | $\gamma$ = 2 |
| Channel parameters | $m_{h_{d_1}}$ = 4, $m_{f_1}$ = 4<br>$m_{h_{d_2}}$ = 2, $m_{f_2}$ = 2<br>$m_{g_r}$ = 3, $\Omega_{g_r}$ = 1<br>$\Omega_{h_{d_n}} = \Omega_{f_n} = 1, \forall n \in \{1, 2\}$ |
| Reflection coefficients | $\Gamma_1$ = 0.8, $\Gamma_2$ = 0.3 |
| RIS elements | $M$ = 48 |
| Split factor | $\alpha$ = 0.6 |

### A. Analysis Validation

To corroborate the validity of our mathematical analysis, different parameter configurations are considered. In this regard, Figs. 7(a) and 7(b) present the theoretical and simulation results for both BSNs with varying numbers of RIS elements, $M$, and different reflection coefficient pairs, $(\Gamma_1, \Gamma_2)$. Fig. 7(c) is plotted by taking a sufficiently large value of $m_{f_1}$ and $m_{f_2}$ to emulate a virtual LoS BSNs-RIS link. Moreover, Fig. 7(d) presents the BER results against a varying number of RIS elements, $M$. As evident from the figures, the simulation results closely match the numerical results obtained using the derived BER expressions, thus verifying the validity of the theoretical analysis. Note the performance degradation when $\Gamma_1 = \Gamma_2 = 0.8$, caused by the increased IUI due to non-compliance with the NOMA principle, and the increased separation between the BER curves of BSN-1 and BSN-2 in Fig. 7(d) as the number of elements allocated to BSN-1 are increased. A detailed description of the effect of reflection coefficient pairs and split factor on the BER performance is provided in Sec. IV-C and IV-E, respectively. The minor discrepancy between the two at high SNR regime occurs because of the requirement of a large sample size, i.e., $(M > 30)$ imposed by the CLT-based Gaussian approximation of the backward channel. However, due to high computational cost, $M_1$ is taken to be 15 and 26, respectively, for the results given in Figs. 7(a) and 7(b).

The comparison of symbol error rate (SER) curves for BSNs employing QPSK modulation against BPSK is presented in Fig. 6. It can be observed that the probability of correct symbol detection is worse for the QPSK scheme compared to BPSK, and an excess of 5 dB SNR is required, on average, for the QPSK system to achieve the same SER performance as that of BPSK. For instance, to achieve an error probability of $10^{-2}$ with $M = 24$ reflecting elements at the RIS, the transmit SNRs required for BSN-1 and BSN-2 are 12.5 dB and 14.5 dB, respectively, for BPSK, and 17.2 dB and 18.8 dB for QPSK. Furthermore, owing to enhanced channel gains with the increasing number of RIS elements, the QPSK scheme with $M = 48$ elements outperforms the BPSK scheme with $M = 24$ at the high SNR regime.

### B. Performance Evaluation of RIS-NOMA-BackCom and Conventional NOMA-BackCom System

In Fig. 8, we compare the RIS-enhanced NOMA-BackCom system with the conventional NOMA-BackCom system for a total of 20 BSNs, i.e., $N = 20$, deployed systematically within the coverage area. We note that the RIS-NOMA-BackCom system is superior to its no-RIS counterpart, even without the optimal values of reflection coefficients. This is due to the fact that the signals reflected by the RIS are coherently combined with the signals arriving through the direct path at the BR, resulting in a stronger overall signal and consequently, a higher SNR value. As a result of this, the BER of the RIS-assisted system is significantly enhanced.

### C. Effects of Reflection Coefficients

The selection of the reflection coefficient pair is a decisive factor of the system performance. Fig. 9 demonstrates the BER performance of both BSNs against the reflection coefficient of BSN-2, $\Gamma_2$, whereas $\Gamma_1$ is set to 1. It can be seen that a large difference between the BSNs' reflection coefficients improves the overall performance due to the effective application of the NOMA scheme, irrespective of the value of $M$, because a lower value of $\Gamma_2$ presents reduced IUI in the detection of BSN-1's symbol, which corresponds to the lower BER performance of BSN-1. Consequently, this selection improves the performance of BSN-2 as well due to a higher probability of successful SIC operation. However, the overall performance deteriorates when $\Gamma_2 < 0.4$, owing to the significant reduction in the signal strength of BSN-2 which raises the likelihood of a decoding error.

On top of the data transmission rate, energy efficiency, and deployment cost, BSNs' coverage range is one of the main concerns for future IoT network deployments. In this regard, Fig. 10 investigates the coverage range of BSNs for different values of the reflection coefficient of BSN-2, $\Gamma_2$, with $\Gamma_1 = 1$. The result shows that the optimal coverage is achieved when the value of $\Gamma_2$ is approximately one-half the value of $\Gamma_1$. For instance, the QoS requirement of $10^{-5}$ BER for both BSNs at a coverage range of 55 meters could be achieved by setting $\Gamma_2 = 0.4$. The optimal reflection coefficient values for other configurations can also be obtained in the same manner.

### D. Comparison of OMA- and NOMA-based Transmissions

Fig. 11 demonstrates the increment in the number of effectively transmitted bits by the inclusion of an RIS in the conventional BackCom system. It can be seen that NOMA performs better than the OMA scheme, as it enables the simultaneous transmission of two symbols to the BR within a single transmission slot, despite the fact that NOMA incurs IUI in its decoding process. However, as illustrated by the number of effectively decoded bits for BSN-1 and BSN-2 in

This article has been accepted for publication in IEEE Transactions on Vehicular Technology. This is the author's version which has not been fully edited and content may change prior to final publication. Citation information: DOI 10.1109/TVT.2024.3440396



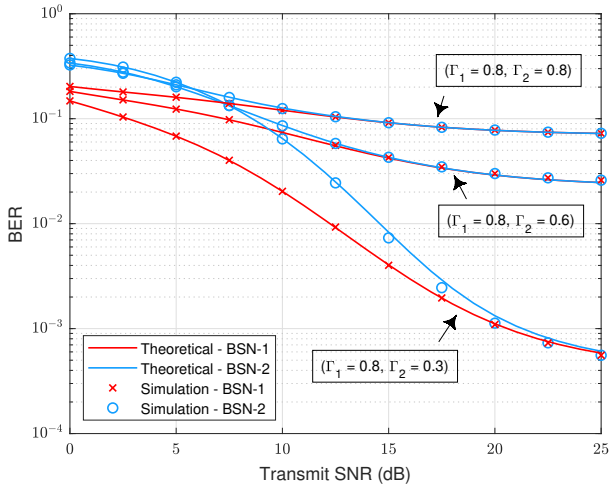


(a) $M = 24$.

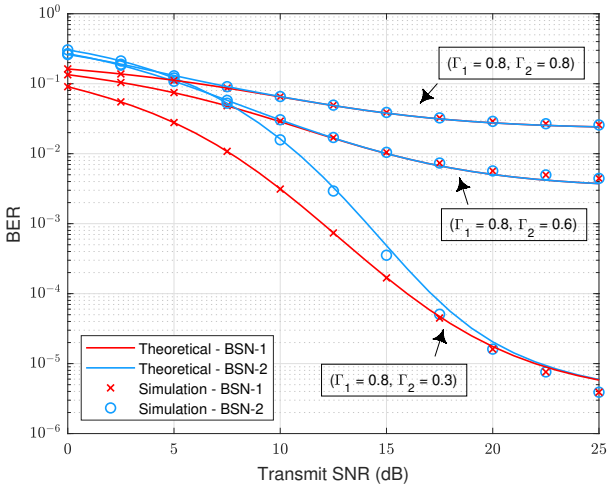


(b) $M = 42$.

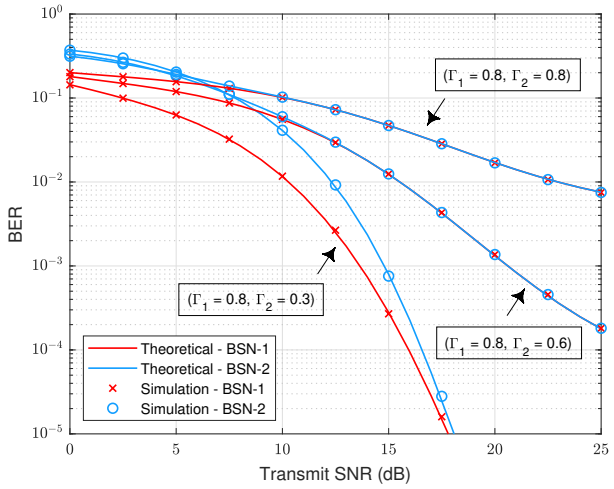


(c) $M = 24$.

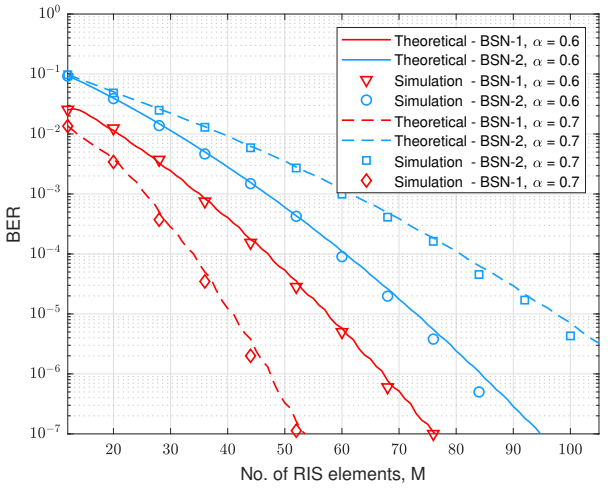


(d) SNR $= 10$ dB, RIS coordinates: $(60, 0)$.

Fig. 7. BER performances of BSN-1 and BSN-2 for the fading configuration ($m_{f_1} = 4$, $m_{h_{d_1}} = 4$, $\Omega_{h_{d_1}} = 1$, $m_{f_2} = 2$, $m_{h_{d_2}} = 2$, $\Omega_{h_{d_2}} = 1$, $m_{g_r} = 3$), and fading-free scenarios.

the RIS-NOMA-BackCom system and the autonomous BSN in RIS-OMA-BackCom system, the individual BSN performance of RIS-OMA-BackCom is better than the corresponding BSN-1 performance of the NOMA counterpart due to the fact that $M$ RIS elements allocated to the exclusive BSN, as opposed to $M_1$ element configuration for BSN-1. Nevertheless, NOMA proves to be spectrally efficient and outperforms OMA by enabling multiple BSNs to communicate using the same resource block.

### *E. Effects of Elements Splitting*

One of the primary determinants of the RIS-assisted system performance is the number of RIS elements allocated to each BSN. Accordingly, Fig. 12 presents the BER contour plot for both BSNs with varying numbers of RIS elements, $M$, and different split factor values, $\alpha$. It can be observed that an increase in $\alpha$ improves the BER performance of BSN-1 due to the allocation of more elements to BSN-1 than BSN-2, irrespective of the value of $M$. This results in a larger difference in the received signal strength at both BSNs. Accordingly, BSN-1's signal undergoes a lower IUI in its decoding process, thereby increasing the likelihood of successful detection of BSN-1's symbol. Moreover. as the error propagation from the SIC decoding process is less likely, BSN-2's BER performance improves as well.

In spite of the low error propagation probability, the performance of BSN-2 degrades if $\alpha$ surpasses the optimal value. This is due to the fact that an increment in $\alpha$ beyond its optimal value significantly reduces BSN-2's signal strength, which results in an increased probability of a decoding error. Also, it has been shown that the optimal split factor is $0.6$ at a transmit SNR of $5$ dB, as the BERs are minimized for both BSNs.

This article has been accepted for publication in IEEE Transactions on Vehicular Technology. This is the author's version which has not been fully edited and content may change prior to final publication. Citation information: DOI 10.1109/TVT.2024.3440396



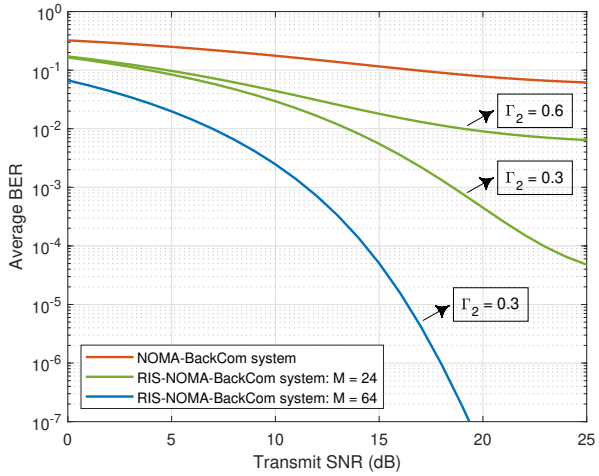


Fig. 8. Performance comparison of the conventional NOMA-BackCom and RIS-NOMA-BackCom, when $\Gamma_1 = 0.8$ and $\alpha = 0.6$.

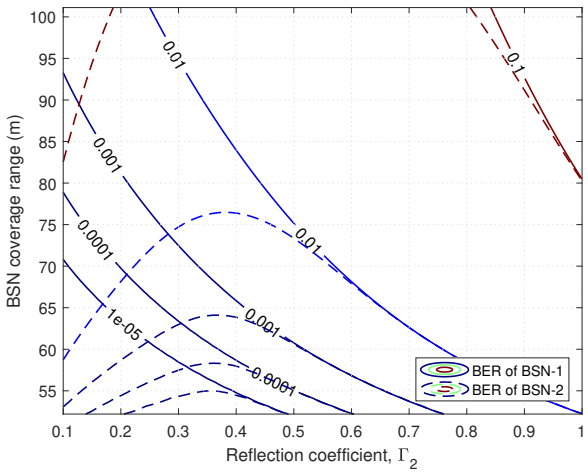


Fig. 10. BER contour plot of BSN coverage range against $\Gamma_2$ with $\Gamma_1 = 1$ and $M = 48$.

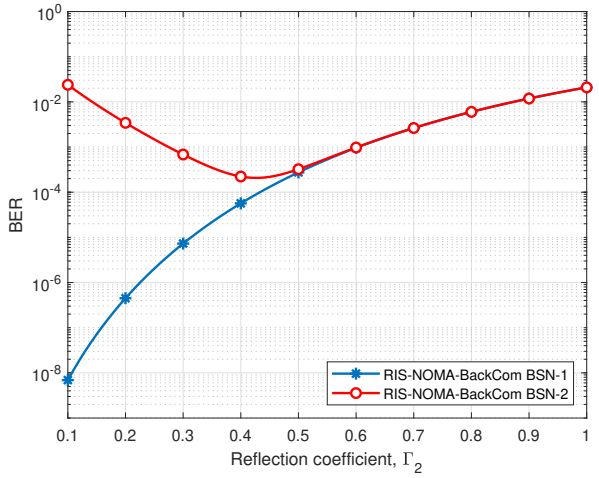


Fig. 9. BER plot against the reflection coefficient of BSN-2, $\Gamma_2$, with $\Gamma_1 = 1$, $M = 48$, and SNR = 10 dB.

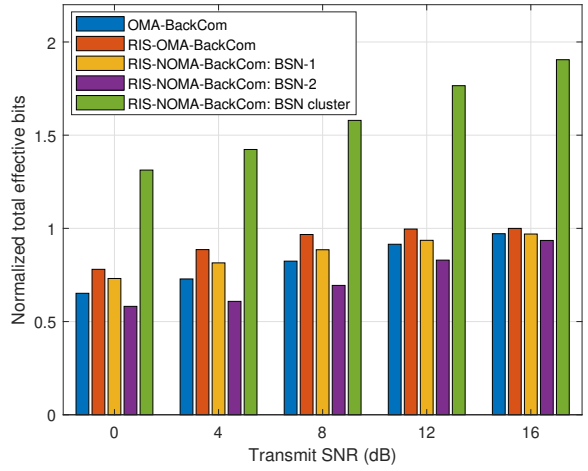


Fig. 11. The normalized effective bits transmitted in a single time slot using OMA and NOMA with $\gamma = 3$ and $M = 24$.

## V. Conclusions

In this work, we investigated the design and BER performance of a multi-cluster NOMA-enabled RIS-assisted bistatic BackCom system for enabling next-generation IoT networks. We derived the BER expressions for a 2-BSN NOMA cluster considering imperfect SIC and RIS elements splitting approach. Moreover, we approximated the PDF of the sum of a Gamma and Nakagami-$m$ RV via MoM. Our simulation results endorsed the analytical results under different channel configurations. Furthermore, our results elucidated the substantial performance improvement realized by integrating an RIS in the conventional NOMA-BackCom system and illustrated that the overall system performance can be greatly enhanced by selecting the optimal reflection coefficient pair and increasing the number of RIS elements. For this reason, future extensions of this work include an optimization analysis, in which the reflection coefficients and the split factor are optimized jointly to maximize the system's BER performance. The analysis of CE-BSNs links, modeled as stochastic fading channels under a weak LoS assumption, is also worth investigating. Furthermore, we aim to investigate the performance of an ambient BackCom configuration and simultaneously transmitting and reflecting RIS (STAR-RIS) for the adaptive configuration of wireless environments [42].

## Appendix
## K-S test for the sum of a Nakagami-$m$ and Gamma RV

A pseudorandom number routine is called $N$ times to accumulate samples $\{y_1, y_2, y_3 \cdots y_N\}$ of the RV $Y$ for computation of its empirical CDF, $\hat{F}_Y(y)$. The hypothesized CDF is that of the Gamma distribution, $F_S(s)$. The null hypothesis for testing assumes no dissimilarity between the theoretical and empirical CDFs, i.e.,

$$H_0 : \hat{F}_Y = F_S,$$

$$H_1 : \hat{F}_Y \neq F_S.$$

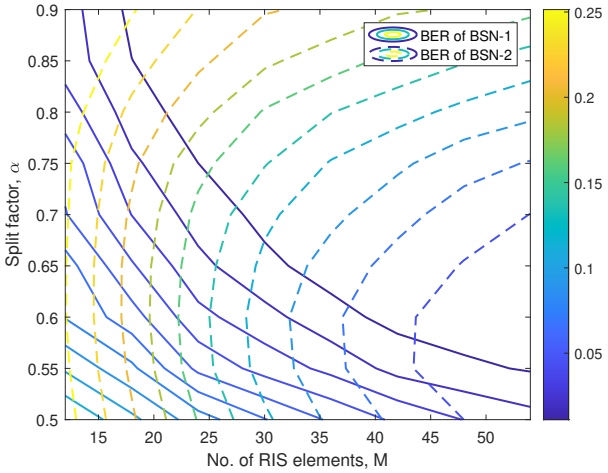


Fig. 12. BER contour plot for varying values of the number of RIS elements, $M$, and split factor, $\alpha$, with SNR = 5 dB.

The null hypothesis is rejected when the test statistic $D_f > D_{crit}$, where the Kolmogorov–Smirnov (K-S) test statistic is defined as

$$D_f = \sup_y \left| \hat{F}_Y(y) - F_S(y) \right|, \tag{49}$$

where sup is the supremum of the set of distances between the two CDFs. Essentially, this test statistic returns the largest absolute difference between the empirical and theoretical CDFs across all $y$ values. The critical value at 5% level of significance is given by

$$D_{crit,\,0.05} = \frac{1.36}{\sqrt{N}},$$

which for $N = 5000$ comes out to be 0.0192. The test is conducted for three different sets of parameters characterizing the Nakagami-$m$ and Gamma distribution modeling the direct and RIS-reflected link, respectively, i.e., $\{M = 8,\, m_{h_d} = 2,\, \Omega_{h_d} = 1,\, m_f = 4,\, m_{g_r} = 3\}$, $\{M = 16,\, m_{h_d} = 2,\, \Omega_{h_d} = 1,\, m_f = 4,\, m_{g_r} = 3\}$ and $\{M = 24,\, m_{h_d} = 3,\, \Omega_{h_d} = 2,\, m_f = 5,\, m_{g_r} = 3\}$, and the test statistic corresponding to each set, calculated using (49), is given as

$$D_f = 0.0115 \text{ for } M = 8, m_{h_d} = 2, \Omega_{h_d} = 1, m_f = 4, m_{g_r} = 3,$$
$$D_f = 0.0086 \text{ for } M = 16, m_{h_d} = 2, \Omega_{h_d} = 1, m_f = 4, m_{g_r} = 3,$$
$$D_f = 0.0139 \text{ for } M = 24, m_{h_d} = 3, \Omega_{h_d} = 2, m_f = 5, m_{g_r} = 3.$$

Since $D_f \leq D_{crit,\,0.05}$ in each case, we fail to reject $H_0$ at the specified significance level. Hence, Gamma distribution closely bears a resemblance to the distribution of the sum of Gamma and Nakagami-$m$ RVs, and can estimate the RV $Y$.

## REFERENCES


[1] M. Usman, S. Basharat, H. Pervaiz, S. A. Hassan, and H. Jung, "On the BER performance of RIS-enhanced NOMA-assisted backscatter communication under Nakagami-m fading," in *Proc. 42nd IEEE Int. Conf. Distrib. Comput. Syst. Workshops (ICDCSW)*, Bologna, Italy, July 2022, pp. 163–168.

[2] W. Saad, M. Bennis, and M. Chen, "A vision of 6G wireless systems: Applications, trends, technologies, and open research problems," *IEEE Netw.*, vol. 34, no. 3, pp. 134–142, May/June 2020.

[3] D. C. Nguyen *et al.*, "6G internet of things: A comprehensive survey," *IEEE Internet Things J.*, vol. 9, no. 1, pp. 359–383, Jan. 2022.

[4] M. Z. Chowdhury, M. Shahjalal, S. Ahmed, and Y. M. Jang, "6G wireless communication systems: Applications, requirements, technologies, challenges, and research directions," *IEEE Open J. Commun. Soc.*, vol. 1, pp. 957–975, July 2020.

[5] A. W. Nazar, S. A. Hassan, H. Jung, A. Mahmood, and M. Gidlund, "BER analysis of a backscatter communication system with non-orthogonal multiple access," *IEEE Trans. Green Commun. Netw.*, vol. 5, no. 2, pp. 574–586, June 2021.

[6] S. Bi, C. K. Ho, and R. Zhang, "Wireless powered communication: Opportunities and challenges," *IEEE Commun. Mag.*, vol. 53, no. 4, pp. 117–125, Apr. 2015.

[7] B. Clerckx, K. Huang, L. R. Varshney, S. Ulukus, and M.-S. Alouini, "Wireless power transfer for future networks: Signal processing, machine learning, computing, and sensing," *IEEE J. Sel. Topics Signal Process.*, vol. 15, no. 5, pp. 1060–1094, Aug. 2021.

[8] A. Bletsas, P. N. Alevizos, and G. Vougioukas, "The art of signal processing in backscatter radio for $\mu$W (or less) internet of things: Intelligent signal processing and backscatter radio enabling batteryless connectivity," *IEEE Sig. Proc. Mag.*, vol. 35, no. 5, pp. 28–40, Sept. 2018.

[9] J.-P. Niu and G. Y. Li, "An overview on backscatter communications," *J. Commun. Inf. Netw.*, vol. 4, no. 2, pp. 1–14, June 2019.

[10] R. Torres *et al.*, "Backscatter communications," *IEEE J. Microw.*, vol. 1, no. 4, pp. 864–878, Oct. 2021.

[11] J. Kimionis, A. Bletsas, and J. N. Sahalos, "Increased range bistatic scatter radio," *IEEE Trans. Commun.*, vol. 62, no. 3, pp. 1091–1104, Mar. 2014.

[12] X. Lu, D. Niyato, H. Jiang, D. I. Kim, Y. Xiao, and Z. Han, "Ambient backscatter assisted wireless powered communications," *IEEE Wireless Commun.*, vol. 25, no. 2, pp. 170–177, Apr. 2018.

[13] Q. Wu and R. Zhang, "Towards smart and reconfigurable environment: Intelligent reflecting surface aided wireless network," *IEEE Commun. Mag.*, vol. 58, no. 1, pp. 106–112, Jan. 2020.

[14] S. Basharat, S. Ali Hassan, H. Pervaiz, A. Mahmood, Z. Ding, and M. Gidlund, "Reconfigurable intelligent surfaces: Potentials, applications, and challenges for 6G wireless networks," *IEEE Wireless Commun.*, vol. 28, no. 6, pp. 184–191, Dec. 2021.

[15] M. Di Renzo *et al.*, "Smart radio environments empowered by reconfigurable intelligent surfaces: How it works, state of research, and the road ahead," *IEEE J. Sel. Areas Commun.*, vol. 38, no. 11, pp. 2450–2525, Nov. 2020.

[16] S. Basharat, S. A. Hassan, A. Mahmood, Z. Ding, and M. Gidlund, "Reconfigurable intelligent surface-assisted backscatter communication: A new frontier for enabling 6G IoT networks," *IEEE Wireless Commun.*, vol. 29, no. 6, pp. 96–103, Dec. 2022.

[17] X. Jia, J. Zhao, X. Zhou, and D. Niyato, "Intelligent reflecting surface-aided backscatter communications," in *Proc. IEEE Glob. Commun. Conf. (GLOBECOM)*, Taipei, Taiwan, Dec. 2020, pp. 1–6.

[18] X. Jia, X. Zhou, D. Niyato, and J. Zhao, "Intelligent reflecting surface-assisted bistatic backscatter networks: Joint beamforming and reflection design," *IEEE Trans. Green Commun. Netw.*, vol. 6, no. 2, pp. 799–814, June 2022.

[19] W. Zhao, G. Wang, S. Atapattu, T. A. Tsiftsis, and X. Ma, "Performance analysis of large intelligent surface aided backscatter communication systems," *IEEE Wireless Commun. Lett.*, vol. 9, no. 7, pp. 962–966, July 2020.

[20] B. Tahir, S. Schwarz, and M. Rupp, "Outage analysis of uplink IRS-assisted NOMA under elements splitting," in *Proc. IEEE Veh. Technol. Conf.*, Helsinki, Finland, Apr. 2021, pp. 1–5.

[21] J. Guo, X. Zhou, S. Durrani, and H. Yanikomeroglu, "Design of non-orthogonal multiple access enhanced backscatter communication," *IEEE Trans. Wireless Commun.*, vol. 17, no. 10, pp. 6837–6852, Oct. 2018.

[22] J. Zuo, Y. Liu, L. Yang, L. Song, and Y.-C. Liang, "Reconfigurable intelligent surface enhanced NOMA assisted backscatter communication system," *IEEE Trans. Veh. Tech.*, vol. 70, no. 7, pp. 7261–7266, July 2021.

[23] A. Ihsan, W. Chen, M. Asif, W. U. Khan, Q. Wu, and J. Li, "Energy-efficient IRS-aided NOMA beamforming for 6G wireless communications," *IEEE Trans. Green Commun. Netw.*, vol. 6, no. 4, pp. 1945–1956, Dec. 2022.

[24] X. Jia and X. Zhou, "IRS-assisted ambient backscatter communications utilizing deep reinforcement learning," *IEEE Wireless Commun. Lett.*, vol. 10, no. 11, pp. 2374–2378, Nov. 2021.

[25] L. Yang, P. Li, Y. Yang, S. Li, I. Trigui, and R. Ma, "Performance analysis of RIS-aided networks with co-channel interference," *IEEE Commun. Lett.*, vol. 26, no. 1, pp. 49–53, Jan. 2022.

[26] V. K. Chapala and S. M. Zafaruddin, "Intelligent connectivity through RIS-assisted wireless communication: Exact performance analysis with phase errors and mobility," *IEEE Trans. Intell. Veh.*, vol. 8, no. 10, pp. 4445–4459, Oct. 2023.

[27] I. Trigui, E. K. Agbogla, M. Benjillali, W. Ajib, and W.-P. Zhu, "Bit error rate analysis for reconfigurable intelligent surfaces with phase errors," *IEEE Commun. Lett.*, vol. 25, no. 7, pp. 2176–2180, July 2021.

[28] A. W. Nazar, S. A. Hassan, and H. Jung, "BER analysis of a NOMA enhanced backscatter communication system," in *Proc. IEEE Glob. Commun. Conf. (GLOBECOM)*, Taipei, Taiwan, Dec. 2020, pp. 1–6.

[29] S. Basharat, S. A. Hassan, H. Jung, A. Mahmood, Z. Ding, and M. Gidlund, "On the statistical channel distribution and effective capacity analysis of STAR-RIS-assisted BAC-NOMA systems," *IEEE Trans. Wireless Commun.*, vol. 23, no. 5, pp. 4675–4690, May 2024.

[30] C. Xu, L. Yang, and P. Zhang, "Practical backscatter communication systems for battery-free internet of things: A tutorial and survey of recent research," *IEEE Signal Process. Mag.*, vol. 35, no. 5, pp. 16–27, Sept. 2018.

[31] S. J. Thomas, E. Wheeler, J. Teizer, and M. S. Reynolds, "Quadrature amplitude modulated backscatter in passive and semipassive UHF RFID systems," *IEEE Trans. Microw. Theory Techn.*, vol. 60, no. 4, pp. 1175–1182, Apr. 2012.

[32] M. S. Ali, H. Tabassum, and E. Hossain, "Dynamic user clustering and power allocation for uplink and downlink non-orthogonal multiple access (NOMA) systems," *IEEE Access*, vol. 4, pp. 6325–6343, Aug. 2016.

[33] C. Psomas and I. Krikidis, "Backscatter communications for wireless powered sensor networks with collision resolution," *IEEE Wireless Commun. Lett.*, vol. 6, no. 5, pp. 650–653, Oct. 2017.

[34] Z. Ding, R. Schober, and H. V. Poor, "On the impact of phase shifting designs on IRS-NOMA," *IEEE Wireless Commun. Lett.*, vol. 9, no. 10, pp. 1596–1600, Oct. 2020.

[35] Y.-C. Liang, J. Chen, R. Long *et al.*, "Reconfigurable intelligent surfaces for smart wireless environments: channel estimation, system design and applications in 6G networks," *Sci. China Inf. Sci.*, vol. 64, no. 10, p. 1–21, July 2021.

[36] L. Wei, C. Huang, G. C. Alexandropoulos, C. Yuen, Z. Zhang, and M. Debbah, "Channel estimation for RIS-empowered multi-user MISO wireless communications," *IEEE Trans. Commun.*, vol. 69, no. 6, pp. 4144–4157, June 2021.

[37] P. Wang, J. Fang, H. Duan, and H. Li, "Compressed channel estimation for intelligent reflecting surface-assisted millimeter wave systems," *IEEE Signal Process. Lett.*, vol. 27, pp. 905–909, May 2020.

[38] E. Björnson, O. Özdogan, and E. G. Larsson, "Intelligent reflecting surface versus decode-and-forward: How large surfaces are needed to beat relaying?" *IEEE Wireless Commun. Lett.*, vol. 9, no. 2, pp. 244–248, Feb. 2020.

[39] G. L. Stüber, *Principles of Mobile Communication, 4th Edition*. New York, NY: Springer, 2017.

[40] M. K. Simon and M. S. Alouini, *Digital Communications Over Fading Channels: A Unified Approach to Performance Analysis; 2nd ed.* Wiley, 2005.

[41] B. Tahir, S. Schwarz, and M. Rupp, "Analysis of uplink IRS-assisted noma under Nakagami-m fading via moments matching," *IEEE Wireless Commun. Lett.*, vol. 10, no. 3, pp. 624–628, Mar. 2021.

[42] J. Xu, Y. Liu, X. Mu, and O. A. Dobre, "STAR-RISs: Simultaneous transmitting and reflecting reconfigurable intelligent surfaces," *IEEE Commun. Lett.*, vol. 25, no. 9, pp. 3134–3138, Sept. 2021.


**Muhammad Usman** (S'24) received his B.E. degree in electrical engineering from National University of Sciences and Technology (NUST), Pakistan, in 2022. He is currently pursuing his Ph.D. in electrical engineering at the Australian National University (ANU). His research interests include integrated sensing and communication (ISAC), reconfigurable intelligent surfaces (RISs), backscatter communication (BackCom), and non-orthogonal multiple access (NOMA).

**Sarah Basharat** (S'23) received her B.E. and M.S. degrees in electrical engineering from National University of Sciences and Technology (NUST), Pakistan, in 2019 and 2021, respectively. Currently, she is pursuing her Ph.D. in electrical engineering from NUST. Her research interests include B5G and 6G communication, non-orthogonal multiple access (NOMA), backscatter communication (BackCom), and reconfigurable intelligent surfaces (RISs).

**Syed Ali Hassan** (S'08-M'11-SM'17) received his Ph.D. in electrical engineering from Georgia Tech, Atlanta, in 2011, his M.S. in mathematics from Georgia Tech in 2011, and his M.S. in electrical engineering from the University of Stuttgart, Germany, in 2007, and a B.E. in electrical engineering (highest honors) from the National University of Sciences and Technology (NUST), Pakistan, in 2004. His broader area of research is signal processing for communications. He is currently a Professor with the School of Electrical Engineering and Computer Science (SEECS), NUST, where he is also the Director of the Information Processing and Transmission Research Group, which focuses on various aspects of theoretical communications. He has (co)authored more than 250 publications in international conferences and journals and has organized several special issues/sessions as editor/chair in leading journals/conferences.

**Haris Pervaiz** (Member, IEEE) received the M.Sc. degree in information security from the Royal Holloway University of London, Egham, U.K., in 2005, and the Ph.D. degree from the School of Computing and Communication, Lancaster University, Lancaster, U.K., in 2016. He is currently working as an Associate Professor (Senior Lecturer) with the School of Computer Science and Electronic Engineering, University of Essex, UK.

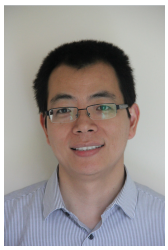

**Zhiguo Ding** (S'03-M'05-F'20) received his B.Eng from the Beijing University of Posts and Telecommunications in 2000, and the Ph.D degree from Imperial College London in 2005. He is currently a Professor in Communications at Khalifa University, and has also been affiliated with the University of Manchester and Princeton University. Dr Ding' research interests are 6G networks, multiple access, energy harvesting networks and statistical signal processing. He is serving as an Area Editor for the *IEEE Transactions on Wireless Communications*, and *IEEE Open Journal of the Communications Society*, an Editor for *IEEE Transactions on Vehicular Technology*, and was an Editor for *IEEE Wireless Communication Letters*, *IEEE Transactions on Communications*, *IEEE Communication Letters* from 2013 to 2016. He recently received the EU Marie Curie Fellowship 2012-2014, the Top IEEE TVT Editor 2017, IEEE Heinrich Hertz Award 2018, IEEE Jack Neubauer Memorial Award 2018, IEEE Best Signal Processing Letter Award 2018, Friedrich Wilhelm Bessel Research Award 2020, and IEEE SPCC Technical Recognition Award 2021. He is a Fellow of the IEEE, a Distinguished Lecturer of IEEE ComSoc, and a Web of Science Highly Cited Researcher in two categories 2022.

**Haejoon Jung** (S'08-M'14-SM'21) received the B.S. degree (Hons.) in electrical engineering from Yonsei University, Seoul, South Korea, in 2008, and the M.S. and Ph.D. degrees in electrical engineering from the Georgia Institute of Technology (Georgia Tech), Atlanta, GA, USA, in 2010 and 2014, respectively. From 2014 to 2016, he was a Wireless Systems Engineer at Apple, Cupertino, CA, USA. From 2016 to 2021, he was with Incheon National University, Incheon, South Korea. Since September 2021, he has been with the Department of Electronic Engineering, Kyung Hee University, as an Associate Professor. His research interests include communication theory, wireless communications, wireless power transfer, and statistical signal processing. He was a recipient of the Haedong Young Scholar Award from the Korean Institute of Communications and Information Sciences, He is serving as an Associate Editor for *IEEE Transactions on Vehicular Technology*, *IEEE Transactions on Aerospace and Electronic Systems*, *IEEE Communications Letters*, *IEEE Wireless Communications Letters*, and ICT Express.